Astron. Astrophys. 357, 637–650 (2000)

ASTRONOMY AND ASTROPHYSICS

SCUBA imaging of high mass star formation regions

J. Hatchell[1], **G.A. Fuller**[1], **T.J. Millar**[1], **M.A. Thompson**[2], **and G.H. Macdonald**[2]

[1] Department of Physics, UMIST, P.O. Box 88, Manchester M60 1QD, UK
[2] Electronic Engineering Laboratory, University of Kent, Canterbury, Kent CT2 7NT, UK

Received 7 September 1999 / Accepted 3 March 2000

Abstract. We present 450 and 850μm images of five ultracompact HII regions (G10.47, G12.21, G13.87, G31.41 and G43.89) taken at $9''/15''$ resolution with SCUBA on the JCMT, and photometric measurements of the central sources at 1350 and 2000μm. We confirm that the sources have high submillimetre fluxes as expected from their IRAS fluxes at 100μm and molecular line emission. Each submillimetre image peaks towards the UCHII regions. Three sources (G10.47, G12.21 and G31.41) have particularly strong central peaks. These peaked sources, which can be easily identified from radial profiles, were previously identified from spectral line surveys as containing hot molecular cores. The non-peaked sources G13.87 and G43.89 do not have hot molecular cores. Using the DUSTY radiative transfer code, we model both the spectral energy distributions and radial profiles of the sources using a combination of $r^{-3/2}$ density profile envelopes plus, for the peaked sources, compact high optical depth cores. Although previous modelling of the SED of UCHII regions has been achieved with constant density shells, we find that $r^{-3/2}$ density profiles are necessary to fit the submm radial emission profiles of these sources. In agreement with previous modelling, we find that the inner radius of the dust shells is larger than would be expected from dust sublimation; the physical mechanism for this is unknown. Two sources (G10.47 and G12.21) have additional peaks within the $2.5'$ SCUBA field of view which are not known to contain UCHII regions and may contain high mass protostars.

Key words: stars: formation – ISM: clouds – ISM: dust, extinction – ISM: H II regions – submillimeter

1. Introduction

Ultracompact HII (UCHII) regions identify recently-formed massive stars. In many cases, their immediate environment still contains the remnants of the natal molecular cloud, so the conditions under which star formation occurred can be studied. In addition, as massive stars are believed to form in clusters, the environments of UCHII regions are a good place to look for massive protostars.

Send offprint requests to: J.Hatchell@umist.ac.uk

Submillimetre dust emission is a good tracer of column density in star formation regions as it rarely becomes optically thick. Here we present observations of the distribution of warm dust surrounding five UCHII regions, mapped at submillimetre (submm) wavelengths using the Submillimetre Common-User Bolometer Array (SCUBA) on the James Clerk Maxwell Telescope (JCMT). SCUBA has a $2.5'$ field of view allowing us to quickly map the dust distribution over the few parsecs surrounding the UCHII regions at moderate resolution ($9''/15''$ at 450/850μm respectively). With the high sensitivity of SCUBA we can detect dust over several orders of magnitude of column density, and investigate the density distribution of the clouds surrounding the UCHII regions.

Spectral energy distributions (SEDs) play a vital part in any determination of the properties of dust surrounding UCHII regions. The SEDs of these sources, which were first collected by Wood & Churchwell (1989; hereafter WC89) have lacked good measurements in the submm part of the spectrum, between the IRAS 100μm datapoint and the 1300μm results of Chini et al. (1986a,b). The SCUBA fluxes at 450 and 850μm fill this gap, and add additional photometry at 1350 and 2000μm.

The sources (G10.47, G12.21, G13.87, G31.41 and G43.89) were selected for their emission from hot, dense molecular gas, as we expect correspondingly strong dust emission. The sources have all been detected previously in high-excitation ammonia (Cesaroni et al. 1992; Olmi et al. 1993), indicating the presence of hot, dense gas. Our molecular line survey towards these (and other) UCHII regions confirmed that several have hot molecular cores, characterised by extremely high column densities and temperature and a rich chemistry with many emission lines (Hatchell et al. 1998a). Interferometric observations have shown that some sources have compact molecular cores which may be separated from the UCHII regions themselves (Cesaroni et al. 1994b). These sources have not been imaged before in the far IR or submm, except with the low resolution of IRAS, although Hoare et al. (1991) obtained flux measurements and cross scans of G10.47 at 350 and 850μm.

In Sect. 2 we describe the observations and data reduction procedure, and present the results. We discuss the images in Sect. 3. In Sect. 4 we model the spectral energy distributions and radial profiles of the sources using the DUSTY code to solve the radiative transfer problem (Ivezić & Elitzur 1997; Ivezić et

Table 1. Observing parameters

wavelength	450μm	850μm	1350μm	2000μm
chop throw	$2'$		$2'$	
int. time	64×1s		9×1s	
beam FWHM	$9''$	$15''$	$22''$	$34''$
zenith opacity	1.9–2.6	0.34–0.43	0.12–0.42	0.08–0.27

Table 2. Source positions and assumed distances (from Churchwell et al. 1990b).

Object	RA (1950)			Dec (1950)			d
	[h	m	s]	[°	′	″]	[kpc]
G10.47+0.03	18	05	40.3	−19	52	21	5.8
G12.21−0.10	18	09	43.7	−18	25	09	13.5
G13.87+0.28	18	11	41.8	−16	46	40	4.4
G31.41+0.31	18	44	59.4	−01	16	04	7.9
G43.89−0.78	19	12	02.8	09	17	19	4.2

al. 1997). Sect. 5 contains a discussion of the modelling results, their implications for the source properties and a comparison with the molecular line data. Sect. 6 contains our conclusions.

2. Observations and data reduction

Observations were made on August 13–15, 1997, using the Submilimetre Common-User Bolometer Array (SCUBA) on the James Clerk Maxwell Telescope (Holland et al. 1999). Observations consisted of simultaneous 450/850μm maps and additional single-pixel photometry at 1350 and 2000μm. The SCUBA array covers a hexagonal $2.5'$ field of view with 91 and 37 pixels at 450/850μm respectively. Maps are fully sampled using the 'jiggle' mode, in which the telescope beam is moved around a 64-position pattern by the secondary mirror in order to fully sample the sky with the wider intrinsic beam spacing of the array. Observing parameters are given in Table 1. Table 2 gives source positions and distances (from Churchwell et al. 1990b)

We reduced the data using the SCUBA User Reduction Facility (SURF; Jenness & Lightfoot 1998). The resulting images are shown in Figs. 1. The maps were calibrated from skydips and observations of Uranus as described in Sandell (1997). Fluxes for each source are given in Table 3. At 450 and 850μm we give both the single beam fluxes towards the peak and fluxes integrated over the entire $2.5'$ SCUBA field of view, except for G12.21 where the $2'$ chop throw results in positive and negative components for sources located near the edge of the image, and only the $1'$ square region encompassing the central source was included. The flux for G10.47 is the total of the three condensations visible in the image. We note that for G10.47 the 350μm and probably also the 800μm fluxes of Hoare et al. (1991) are low compared to our 450 and 850μm fluxes, taking the wavelength difference into account, probably because we have integrated over a larger region. Uncertainties in the fluxes are dominated by uncertainties in the sky transmission, which varied substantially over the course of the observations. Estimates of the flux uncertainties from the Uranus observations are 5% and 20% at 850 and 450μm respectively. At 1350/2000μm, from the opacities uncertainties were 5% on 14 August (G10.47, G43.89) and 20% on 15 August (G12.21, G13.87, G31.41) (due to poorer weather). The beam was measured using observations of Uranus, and consisted of a roughly Gaussian main beam, with FWHM given in Table 1 plus an extended error lobe, which contained roughly 15% and 50% of the flux at 850 and 450μm respectively. Fig. 2 shows images of Uranus at both wavelengths. Because of the extended error lobe, we did not attempt any beam deconvolution. Instead, when comparing the images with models (see Sect. 4) we convolved the models with the maps of Uranus, assuming it to be a point source. In the case of a simple Gaussian deconvolution, the correction for Uranus's finite ($3.8''$) diameter to the main beam FWHM of $9''/15''$ is less than $1''$, and with much of the flux in the extended error beam at 450μm the correction would be difficult to apply.

The observations were taken with a $2'$ chop throw. Given the extended nature of these sources, which are embedded in molecular cloud complexes (Scoville et al. 1987), the off positions will not have been entirely free of emission, and this will have been subtracted from the fluxes and as a background from the images. The fluxes are therefore strictly lower limits on the total flux in the $2.5'$ SCUBA field of view. However, as we are most interested in the warmer dust corresponding to the warm cores which are seen by IRAS, the background-subtracted flux measurements are appropriate. As the flux in the images have fallen to a few percent of peak at the edge of the map, and there are no strong negative features, either the emission in the off position is negligible or we have subtracted a roughly constant background flux. An exception is G12.21 where we have clearly self-chopped onto the sources to the southeast of the main peak (Fig. 1). In the case of roughly constant background flux, the radial profiles (Sect. 4) trace only the varying component of density. At large radius, the radial profiles may be slightly distorted by this background subtraction process.

3. Images

Images of the 450 and 850μm emission surrounding the five UCHII regions are shown in Fig. 1. Detailed descriptions of each source, and what is known about them from other wavelengths, are given below.

3.1. G10.47

The G10.47+0.03 HII region containing the UCHII regions G10.47+0.03 A, B and C is coincident with the strong submm emission peak in the centre of the map and has been extensively observed at radio wavelengths (Garay et al. 1993b,c; WC89; Becker et al. 1994). G10.47+0.03A is marked with a cross in Fig. 1. This region shows OH, CH_3OH and H_2O maser emission (Caswell et al. 1995a,b,c,d; Caswell et al. 1993; Hofner & Churchwell 1996; Palagi et al. 1993; Braz & Epchtein 1983; Zheng & Ling 1997), and a hot, dense molecular core where many species have been detected (Garay et al. 1993a; Cesaroni et al. 1992, 1994a,b, 1998; Plume et al. 1992; Gen-

Table 3. Measured fluxes at 450 and 850μm (integrated over the entire image) and at 450, 850, 1350 and 2000μm (single pixel). Uncertainties are due to variation in the sky transmission (see Sect. 2).

Source	Flux (Jy)					
	450μm (map)	850μm (map)	450μm ($9''$ beam)	850μm ($15''$ beam)	1350μm ($22''$ beam)	2000μm ($34''$ beam)
G10.47	507 ± 101	80.0 ± 4.0	242 ± 48	40.9 ± 2.0	13.2 ± 0.7	4.4 ± 0.5
G12.21	147 ± 30	27.4 ± 1.4	94 ± 19	13.6 ± 0.7	3.2 ± 0.6	1.1 ± 0.2
G13.87	140 ± 28	27.8 ± 1.4	24 ± 5	5.2 ± 0.3	2.2 ± 0.4	1.5 ± 0.3
G31.41	227 ± 56	55.1 ± 2.8	84 ± 17	27.4 ± 1.4	4.9 ± 1.0	2.9 ± 0.6
G43.89	117 ± 24	22.2 ± 1.1	15 ± 3	3.2 ± 0.2	1.25 ± 0.08	0.66 ± 0.03

sheimer et al. 1996;; Olmi et al. 1993, 1996a,b; Shepherd & Churchwell 1996; Hatchell et al. 1998a,b,c; 1999; Nummelin et al. 1998; Wyrowski et al. 1999). The large scale CO distribution was mapped by Scoville et al. (1987). Hoare et al. (1991) observed and modelled the submm emission from this source.

The southwestern peak lies towards the east section of the HII region G10.46+0.03 (the lowest cross on Fig. 1), close to G10.46+0.03A (Garay et al. 1993b; Becker et al. 1994; Zoonematkermani et al. 1990; Handa et al. 1987), and corresponds to the IRAS 18056-1952 position and a third NH_3 peak (Garay et al. 1993a; Cesaroni et al. 1998). This region has also been extensively studied in molecular lines and also has hot molecular core characteristics (Wouterloot et al. 1993; Bronfman et al. 1996; Shepherd & Churchwell 1996) and associated CH_3OH, OH and H_2O masers (Cohen et al. 1991; Kalenskij et al. 1992; Palagi et al. 1993; Walsh et al. 1997; Zheng & Ling 1997). Chini et al. (1986a,b) measured the 1300μm flux. A trail of small HII regions, detected from 2–20cm and including G10.46+0.03 C and other small sources, extends south to the 1.5' limit of the SCUBA map in the direction of G10.44+0.01 but has no associated warm dust (Furst et al. 1990; Garay et al. 1993b; Griffith et al. 1994; Aliakberov et al. 1985).

The northern submm peak at $\sim 18^{\rm h}\,05^{\rm m}\,40^{\rm s}\,, -19^\circ\,51'\,45''$ shows a compact NH_3 clump (Garay et al. 1993a, marked with a cross on Fig. 1) and OH and CH_3OH masers (Caswell et al. 1995c; Caswell 1998), but no radio emission has been detected at this position, suggesting that any UCHII region is still optically thick; this clump may be at an earlier stage of evolution than either G10.47+0.03 or G10.46+0.03.

3.2. G12.21

The 450 and 850μm maps show a central source with extensions to the northeast and southeast. The main submm peak is associated with the UCHII region G12.21-0.10; this has been detected at several radio wavelengths (WC89; Zoonematkermani et al. 1990; Becker et al. 1994) as well as at 70μm (Jaffe et al. 1982) and JHK (Testi et al. 1998), has OH, CH_3OH and H_2O masers (Braz & Ephchtein 1983; Hofner & Churchwell 1996; Walsh et al. 1997; Palagi et al. 1993; Bachiller et al. 1990; Jaffe et al. 1981), and associated molecular line emission from hot, dense, chemically rich gas (Hatchell et al. 1998a,b; Anglada et al. 1996; Cesaroni et al. 1992,1998; Plume et al. 1992; Churchwell et al. 1990b; Shepherd & Churchwell 1996; Olmi et al. 1993). The large scale CO distribution was mapped by Scoville et al. (1987). The extension to the northeast contains no radio sources, but the extension to the south contains a CH_3OH maser $30''$ to the south of the peak (Caswell et al. 1995c).

To the east and southeast, at the edge of the 850μm map, are two further peaks. These appear as negative features in the northwest of the maps (not visible in Fig. 1) because the $2'$ chop throw has resulted in self-chopping. The eastern peak, G12.21-0.12, has been detected in molecular lines tracing dense, hot gas (Forster et al. 1985; Plume et al. 1992; Anglada et al. 1996) and also has OH, H_2O and CH_3OH masers (Roellig et al. 1999; Forster & Caswell 1989; Caswell 1998; Zheng & Ling 1997; Mehringer et al. 1995; Palagi et al. 1993; Menten 1991; Forster & Caswell 1989; Kemball et al. 1988; Braz & Epchtein 1983; Hofner & Churchwell 1996; Koo et al. 1988) but no known associated radio source, though further observations are needed to confirm this. IRAS 18097-1825A is centred $\sim 15''$ west of this clump.

The southeastern source has been detected at 6 and 11 cm and in hydrogen radio recombination lines (Aliakberov et al. 1985, Lockman 1989) and also has an associated CH_3OH maser (Caswell et al. 1995c). Chini et al. (1986a,b) measured the 1300μm flux centred on this position.

3.3. G13.87

G13.87 appears as a single submm clump. The apparent elongation in the east-northeast/west-northwest direction is the effect of the SCUBA beam. A possible extension to the north appears at 850μm but is not seen at 450μm and is unlikely to be real. Associated with the central peak is the cometary HII region G13.87+0.28 (Garay et al. 1993c, 1994; Becker et al. 1994; Redman et al. 1998; Aliakberov et al. 1985; Wink et al. 1983; Griffith et al. 1994; Lockman 1989; Furst et al. 1990). $40''$ to the north lies a second radio source, G13.874+0.281, detected at 20 cm but undetected by SCUBA (Zoonematkermani et al. 1990). The clump has been detected in several molecular species (Olmi et al. 1993; Cesaroni et al. 1992; Plume et al. 1992; Churchwell et al. 1990b; Anglada et al. 1996; Bronfman et al. 1996; Shepherd & Churchwell 1996; Wouterloot et al. 1993) although it is not chemically rich (Hatchell et al. 1998a). The large scale molecular cloud was mapped in CO by Scoville et al. (1987).

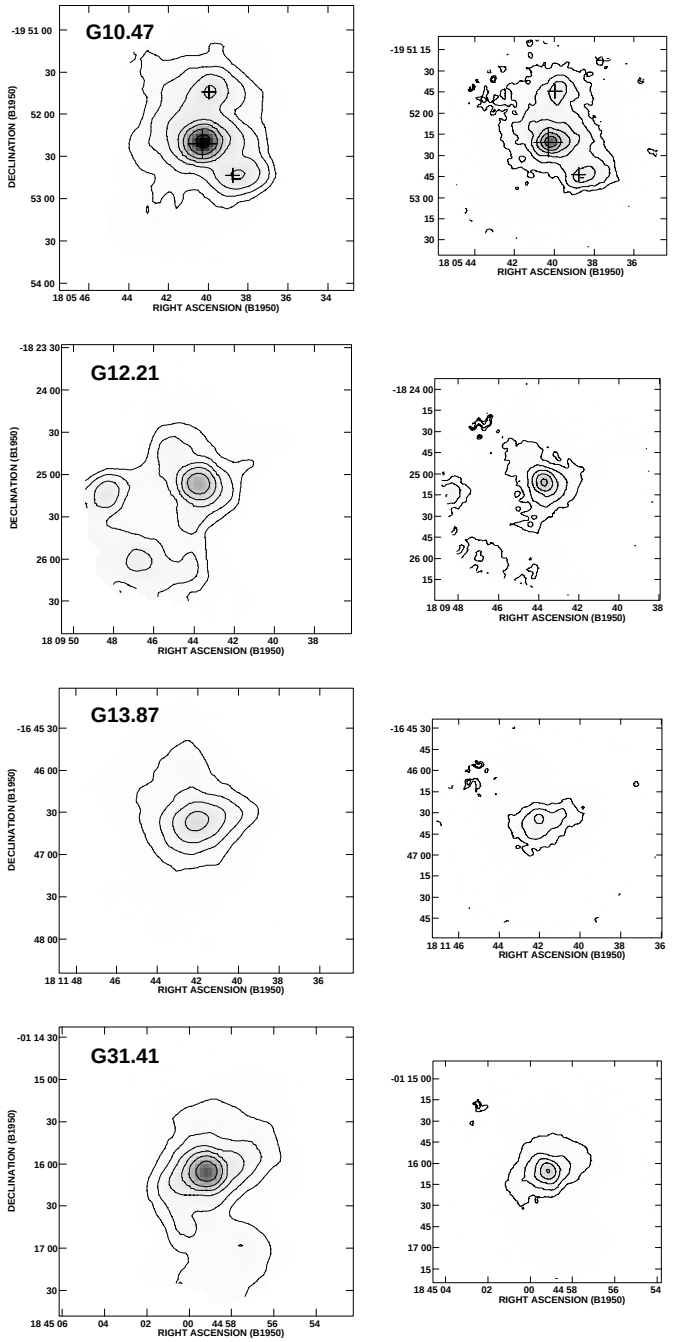

Fig. 1. 850 and 450μm maps. Contours increase in multiples of 2 from 0.5 Jy/beam (850μm, left) or 5 Jy/beam (450μm, right). The base contour is the following percentage of the peak flux: at 850μm, 1% (G10.47) 4% (G12.21), 10% (G13.87), 2% (G31.41) and 16% (G43.89); and at 450μm, 2% (G10.47), 5% (G12.21), 21% (G13.87), 6% (G31.41) and 33% (G43.89). The crosses on the G10.47 map are at the positions of (top to bottom) G10.48+0.03 NH_3 clump, G10.47+0.03A UCHII and G10.46+0.03 UCHII regions (Garay et al. 1993a).

Chini et al. (1986a,b) made a flux measurement at 1300μm; the associated IRAS source is 18116-1646, and it has been extensively studied in the infrared (Kwok et al. 1997; Zavagno et

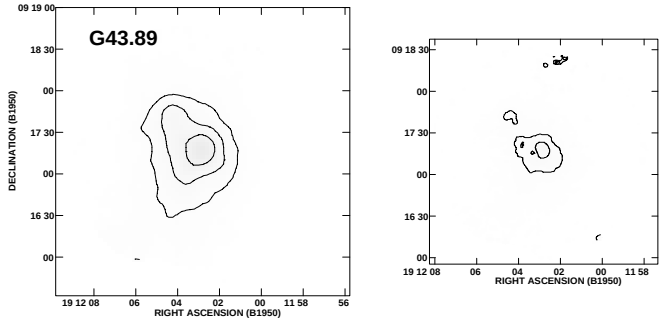

Fig. 1. (continued)

al. 1992; Cox 1990; Jourdain de Muizon et al. 1990; Simpson & Rubin 1990; Volk & Cohen 1989; Jaffe et al. 1981,1982). Maser detections include H_2O (Hofner & Churchwell 1996; Codella et al. 1995; Palagi et al. 1993) and CH_3OH (Walsh et al. 1997; Koo et al. 1988; Braz & Epchtein 1983; van der Walt et al. 1995)

3.4. G31.41

G31.41+0.31 appears as a core-halo UCHII region in the survey of WC89, and has been detected at several radio wavelengths (Becker et al. 1994; Garay et al. 1993c; Wink et al. 1983; Zoonematkermani et al. 1990; Furst et al. 1990; Lockman 1989; Handa et al. 1987; Aliakberov et al. 1985). The submm emission shows one central peak with some extension to the south at 850μm. Again, the west-northwest/east-southeast elongation is likely to be due to the SCUBA beam. However, there are CH_3OH masers detected $20''$ to the west of the submm peak (Walsh et al. 1997; Caswell et al. 1995b,c) and there is a radio detection $40''$ to the east (Aliakberov et al. 1985). The central peak also has associated H_2O, OH and CH_3OH maser emission (Hofner & Churchwell 1996; Tang et al. 1996; Gaylard et al. 1994; Palagi et al. 1993; Schutte et al. 1993; Cohen et al. 1991; Koo et al. 1988; Braz & Epchtein 1983; Gaume & Mutel 1987). The molecular line emission towards the UCHII region is chemically rich and many high-excitation transitions have been detected (Wyrowski et al. 1999; Hatchell et al. 1998a,b,c;1999; Cesaroni et al. 1991, 1992, 1994a,b, 1998; Nummelin et al. 1998; Olmi et al. 1996a,b; Bronfman et al. 1996; Shepherd & Churchwell 1996; Anglada et al. 1996; Tang et al. 1996; Wouterloot et al. 1993; Plume et al. 1992; Churchwell et al. 1990b, 1992; Wyrowski & Walmsley 1996; Gensheimer et al. 1996). Chini et al. (1986a,b) measured the 1300μm flux towards the central peak.

3.5. G43.89

The submm image for G43.89 shows a single peak towards the radio source G43.89-0.78; this is a cometary UCHII region of diameter $4''$ (WC89). H_2O masers have been detected towards the peak (Hofner & Churchwell 1996; Brand et al. 1994), and also CH_3OH and OH masers (Schutte et al. 1993; Bachiller et al. 1990) and it has been the subject of many radio observations (Wood et al. 1988; Zoonematkermani et al. 1990; Handa et al. 1987; Furst et al. 1990; Reich et al. 1990; Aliakberov et

al. 1985; Lockman 1989). The infrared fluxes and spectrum were measured by IRAS (Zavagno et al. 1992; Jourdain de Muizon et al. 1990; Simpson & Rubin 1990; Olnon et al. 1986) and Doherty et al. (1994) carried out 2μm spectroscopy. Some molecular line emission has been detected, but the source is not chemically rich (Hatchell et al. 1998a; Baudry et al. 1997; Bronfman et al. 1996; Shepherd & Churchwell 1996; Churchwell et al. 1990b; Olmi et al. 1993); the large-scale CO distribution was mapped by Scoville et al. (1987). Chini et al. (1986a,b) measured the 1300μm flux.

3.6. Peaked vs. non-peaked sources

In all five sources there is strong submm emission which peaks towards the target UCHII region, within our $9''/15''$ resolution and few arcsecond pointing accuracy. In at least two sources (G10.47 and G12.21) there are also secondary peaks. It is particularly evident at 450μm that three of the sources (G10.47, G12.21 and G31.41) have more pronounced central peaks compared to the surrounding low-level emission (the contour levels are the same for each source). This is also clear from Table 3: roughly $1/2$ the map flux is contained in a single beam centred on the peak for G10.47, G12.21 and G31.41 whereas in G13.87 and G43.89 this figure is less than $1/5$. The difference between peaked and non-peaked sources also can be seen clearly in the radial profiles used for modelling in Sect. 4 (Figs. 5 and 7).

In our spectral line survey towards 14 UCHII regions (Hatchell et al. 1998) we noted that some sources were chemically rich, with many molecular species detected, including grain mantle species and their daughter products. We concluded that these sources contained hot, dense molecular cores. Other sources were line-poor, with only common molecules such as CO, SO, CS and CH_3OH detected. Of the five sources in our SCUBA sample, the three peaked sources, G10.47, G12.21 and G31.41 were all line-rich in the molecular line survey, whereas G13.87 and G43.89 were line-poor. The peaked sources in the SCUBA sample can therefore be identified with the sources with hot molecular cores.

4. Modelling the dust emission

Previously, good fits to the SEDs of similar young high mass sources have been produced using spherically symmetric dust shell models (Chini et al. 1987; Churchwell et al. 1990a (hereafter CWW90); Wolfire & Churchwell 1994; Hoare et al. 1991; Faison et al. 1998). The most successful models have used constant density shells (Chini et al. 1987; CWW90; Faison et al. 1998). These models have large outer radii (a few $\times$ 10^{18}–10^{19}cm) and large inner cavities ($\sim 10^{17}$–10^{18} cm) with a dust temperature at the inner edge of 200–300K. The grain mixture used is a mixture of crystalline carbon and silicate, with the graphite/silicate ratio reduced to about half the standard Mathis et al. (1977) abundances (MRN) in order to fit both the 9.7μm silicate feature and infrared optical depths. Unfortunately there is no overlap between our sample and the list of sources modelled previously; however, WC89 showed that the SEDs for all these UCHII region sources are remarkably similar, and Faison et al. (1998) modelled all 10 sources for which they had sufficient data with shells matching the above description, so we would expect that the SEDs of our sources could also be fitted with this model.

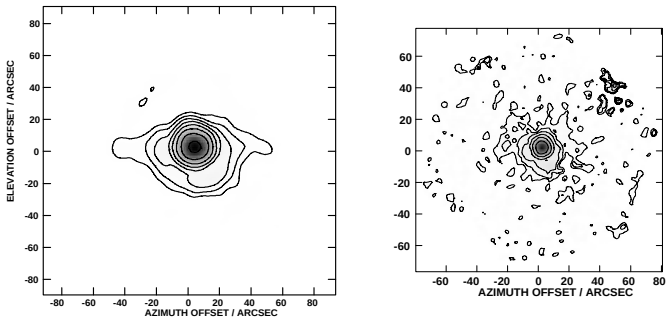

Fig. 2. 850 and 450μm maps of Uranus, showing the SCUBA beam. Contours increase in multiples of 2 from 0.5 Jy/beam (850μm, left) or 3 Jy/beam (450μm, right). The base contour is approximately 1% of the peak flux at both wavelengths.

The submm observations presented here provide not only submm points on the SEDs but also images whch provide structural information, and these additional constraints lead us to try some further modelling of the dust distribution. Following previous work, we model the sources using spherically symmetric shells heated by one or more embedded massive stars. As well as SEDs and submm images, further constraints on the models come from physical conditions derived from molecular line studies and infrared optical depths.

To solve the radiative transfer for spherically symmetric dust shells we used the DUSTY program (Ivezić & Elitzur 1997; Ivezić et al. 1997), which has kindly been made available by the authors. DUSTY requires as input the properties of the central source and the surrounding dust shell – including grain properties, density distribution, temperature at inner radius, and optical depth at specified wavelength – and solves the equation of radiative transfer to find the temperature and the emission as function of radius. It then calculates the resulting spectral energy distribution and radial surface brightness profile.

In order to compare the radial profiles from DUSTY with our observations, we turned the 1D model profiles into 2D surface brightness maps and convolved with maps of Uranus which we take as representative of the telescope beam. Images of Uranus are given in Fig. 2 and the average radial profile is shown in Fig. 3. In creating the 2D maps we assumed a distance to match the source with which we wanted to compare the model. We extracted the 1D average radial flux profiles of the beam-convolved models, and did the same for the observed sources.

The data to which the SEDs are fitted comes from IRAS (12–100μm), the SCUBA observations presented here (450–2000μm), and Chini et al. (1986a,b) (1300μm). We have not attempted to fit the short wavelength (1–5μm) fluxes for these sources (Moorwood & Salinari 1981; Chini et al. 1987). High resolution near-IR observations show clusters of stars surrounding UCHII regions, and the flux in a 10–$15''$ beam is dominated

Table 4. Model parameters as applied to each source: density index $n(r) \propto r^{-p}$, optical depth $\tau_{100\mu m}$, inner and outer radii r_i and r_o, and derived column density and mass. Bolometric luminosities for each source are given in Table 5

source	model	p	$\tau_{100\mu m}$	r_i		r_o		$T_d(r_o)$	N_{H_2}	M^a
				10^{16}cm	arcsec	10^{18}cm	arcsec	K	10^{23}cm^{-2}	$10^4\,M_\odot$
G10.47	$r^{-3/2}$	1.5	0.3	9.5	1.1	9.5	110	17	2.3	
		1.5	0.9	”	”	”	”	15	7.0	3
	core	0	10	6.1	0.7	0.18	2.0	52	78	0.3
	CWW90[b]	0	0.19	9.0	1.0	2.9	33	25	1.5	0.9
G12.21	$r^{-3/2}$	1.5	0.3	14	0.7	14	69	17	2.3	
		1.5	0.9	”	”	”	”	15	7.0	7
	core	0	10	7.7	0.4	0.23	1.1	52	78	0.4
G31.41	$r^{-3/2}$	1.5	0.3	6.2	0.5	19	161	12	2.3	
		1.5	0.9	”	”	”	”	10	7.0	6
	core	0	10	6.1	0.5	0.18	1.5	52	78	0.3
G13.87	$r^{-3/2}$	1.5	0.1	6.2	0.9	4.9	74	20	0.8	
		1.5	0.9	”	”	”	”	16	7.0	1
	CWW90[b]	0	0.19	5.9	0.9	1.9	29	25	1.5	0.4
G43.89	$r^{-3/2}$	1.5	0.1	3.0	0.5	9.0	143	13	0.8	
		1.5	0.9	”	”	”	”	10	7.0	1

[a] Masses for the $r^{-3/2}$ models are for the combined low plus high optical depth combinations described in the text.
[b] CWW90-style flat density model (see Sect. 4.1)

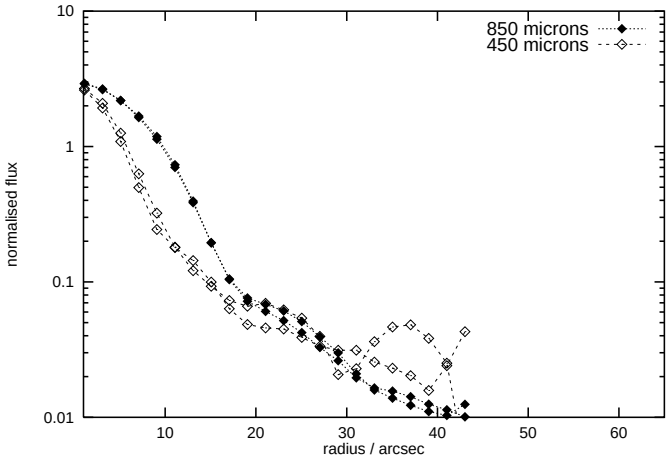

Fig. 3. Uranus radial profiles (azimuthal averages) at 450μm (dashed) and 850μm (dotted). The two profiles at each wavelength correspond to images taken on August 13 and 14.

by stars which are not embedded or powering the UCHII region itself (Feldt et al. 1998, 1999). Spherically symmetric models tend to be optically thick at these wavelengths, whereas models of flattened envelopes or with outflow cavities allow some scattered starlight to reach the observer. Although the near-IR fluxes may be confused by nearby stars, measurements of extinction of the hydrogen recombination lines in the 1–5μm range are a valid constraint, as these are emitted from the UCHII region itself.

In DUSTY the shape of the SED is independent of the luminosity of the central source but to compare with the measured fluxes we scaled the model SEDs to the estimated luminosity of each source. For luminosities we initially used the values in Churchwell et al. (1990b), that is, the bolometric fluxes from IRAS data as calculated by WC89 corrected for the revised distances of Churchwell et al. (1990b). We later adjusted some of the luminosities in order to fit the SEDs better (see Sect. 5).

4.1. Constant density models

In Fig. 4 we show a DUSTY reproduction of the CWW90 best-fit large radius constant density model together with SED data and radial profiles for two sources in our sample, G13.87 and G10.47. The CWW90 model is scaled to appropriate fluxes for our sources (it was chosen to fit another UCHII region source, G5.89). Parameters for this and other models are given in Table 4. These sources were selected for comparison because they have comparable distances (4.4 and 5.8 kpc) but different radial profiles: whereas G10.47 is typical of the strongly peaked sources, with a radial distribution which falls off quickly on small scales, G13.87 has a much flatter distribution, as can be seen in Fig. 4. The fit to the SEDs is reasonable, remembering that the CWW90 model is actually for G5.89 and a better fit to our sources could be obtained by adjusting the radius or column density. However, a large radius constant density shell fails badly to fit the radial profiles in the submillimetre: within the shell ($\sim 30''$) the profile is too flat; further out, it falls off too quickly with radius at 850μm (at 450μm the flux at large radius is a result of the large error beam).

We cannot see how to reconcile the large radius constant density shells which fit the SEDs so well with our submillimetre radial profiles. The form of the radial profiles is largely determined by the chosen density distribution, as this in turn

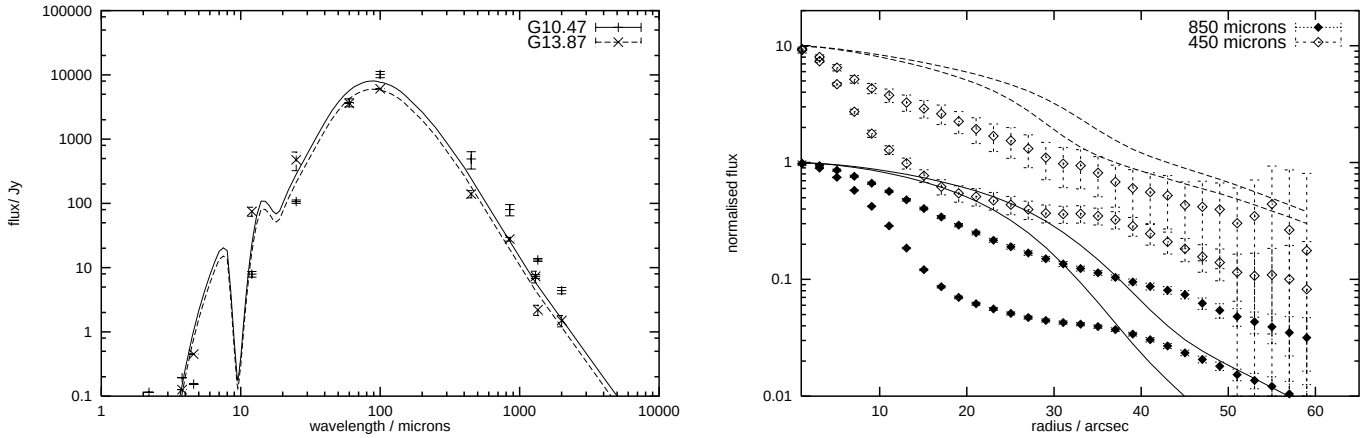

Fig. 4. SED (left) and radial profiles (right) for a flat density distribution source following CWW90, compared with observed fluxes and profiles for G10.47 and G13.87 (errorbars). Profiles at 850μm and 450μm are shown solid and dashed lines respectively. In the plot of profiles, the lower and upper of each pair of curves with the same origin are for G10.47 and G13.87 respectively. The CWW90-type model parameters are given in Table 4

determines the radial temperature distribution. The flat density distributions that have been used to explain the SEDs result in submillimetre profiles that are too shallow. Of the other parameters that can be altered within the range of existing flat density models, increasing the temperature at the inner boundary results in SEDs which peak shortward of 100μm and does not solve the flat profile problem; increasing the outer radius extends the flat profile section further out, making the fit worse; and reducing it produces a sharp falloff which underpredicts the fluxes at large radius (though it produces a good fit to the inner parts of the strongly peaked sources, as we show later).

4.2. $r^{-3/2}$ models

In order to model the submm radial profiles we need to use a steeper density distribution, but this adversely affects the fits to the SEDs. The steeper density distributions have relatively more material close to the star and produce more emission at shorter wavelengths. For example, Hoare et al. (1991) favoured an r^{-2} density distribution which was consistent with their 800μm scans and with densities at large radius but produced an SED which peaked at 70–80μm. As noted by CWW90, in order to have the SED peak at $\sim 100\mu$m, a high optical depth is required which produces too strong a silicate feature and near-IR optical depths at the Brα, Brγ and Pfγ wavelengths which are also higher than observed. Conversely, if the near-infrared part of the spectrum is fitted, then the submm emission is too low and the SED peaks at too short a wavelength.

One way to produce both long and short-wavelength emission is to combine SEDs of different optical depth, considering the sources to have different column densities of dust in different directions, breaking the spherical symmetry. In this way, the observed silicate feature and NIR optical depths can be produced by regions of low opacity and the submm emission by higher optical depth paths. As molecular clouds are observed to be clumpy, and a popular explanation for cometary UCHII regions is that they have formed on the edge of molecular clouds and are expanding into regions of different densities on each side (Tenorio-Tagle et al. 1977; Dyson et al. 1995; Redman et al. 1996; Williams et al. 1996; Lizano et al. 1996), it seems reasonable that the dust optical depth should vary with direction.

The radiative transfer code calculates for spherically symmetric geometry only. In order to model a non-spherical case, we have had to make an approximation: for the purpose of modelling, we assume that the different optical depth components do not obscure each other. This allows us to add their SEDs without modification. What we have modelled is a geometry where these components do not shadow each other - strictly, where the components are like segments of an orange viewed from the stem. A more realistic simple geometry would be a high optical depth sphere/torus with conical regions of low optical depth (perhaps cleared by a bipolar flow). In an orientation where one cone is forward-facing, there is little shadowing by the surrounding material, and our model is a good approximation to this scenario.

We first consider the sources with the flattest distributions in our sample - the non-peaked sources G13.87 and G43.89 - and look at the radial profiles to determine the density distribution. In Sect. 4.4 we shall see that neither r^{-1} or r^{-2} models are consistent with the radial profiles. Here we note that a $r^{-3/2}$ density distribution fits very well. Fig. 5 shows the submm profiles for $r^{-3/2}$ shells compared to the measured profiles for G13.87 and G43.89. Fig. 5 also shows that by combining two $r^{-3/2}$ partial shells with 100μm optical depths of 0.1 and 0.9, we can also produce acceptable fits to the SEDs. The composition of the SED is shown for G13.87.

We are not concerned about the small discrepancies that remain between the models and the data, as several further sources of uncertainty are not represented in the errorbars. The errorbars on the SED do not take into account the fact that different measurements were taken with different pointing centres and with different beam sizes, though the $2.5'$ field of view over which

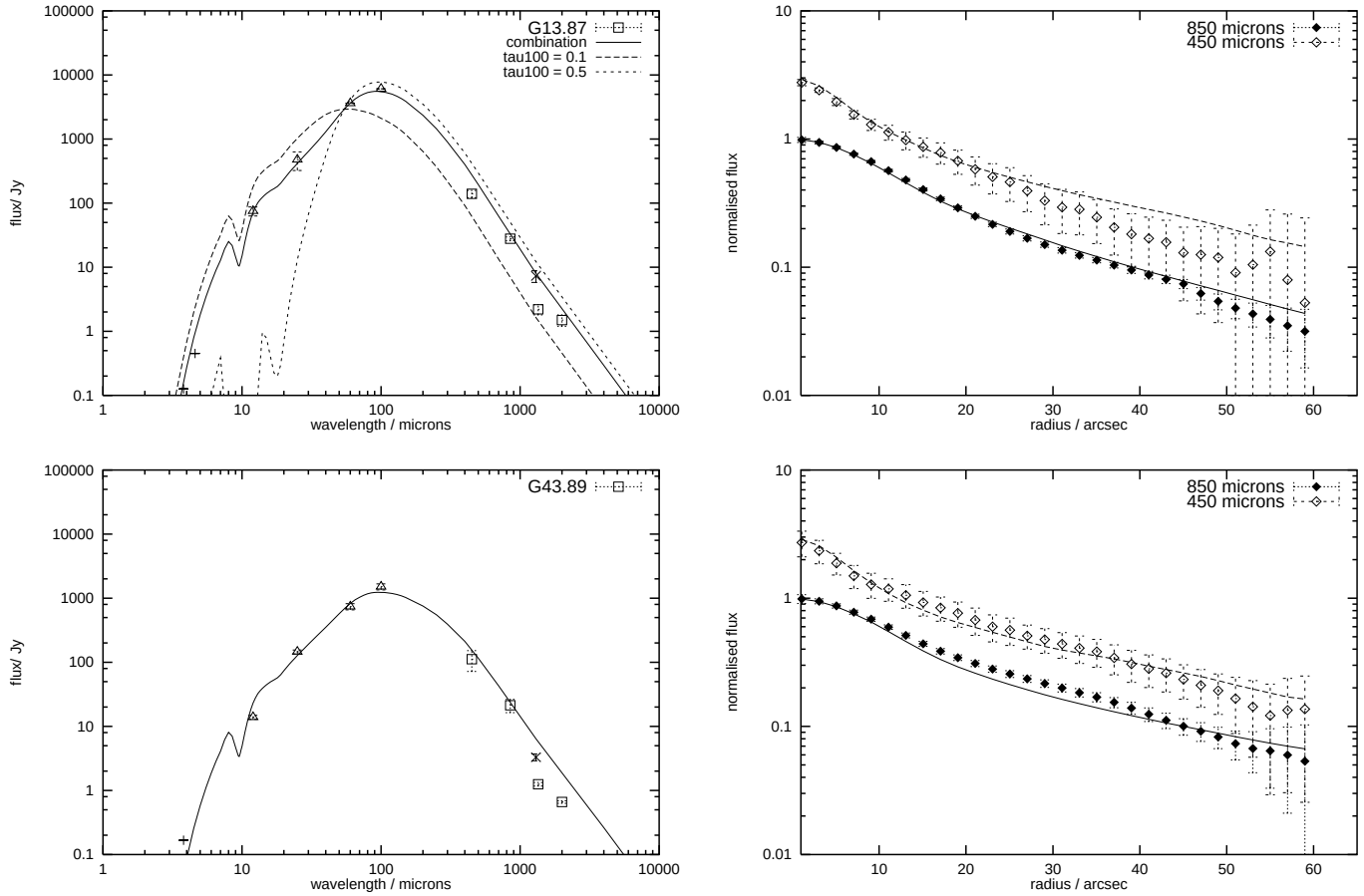

Fig. 5. SEDs and radial profiles for the non-peaked sources G13.87 (top) and G43.89 (bottom), fitted by $r^{-3/2}$ density distributions. The SED for both G13.87 and G43.89 is the combination of $r^{-3/2}$ $\tau_{100\mu\mathrm{m}} = 0.1$ and $\tau_{100\mu\mathrm{m}} = 0.9$ models given in Table 4. These components are shown individually for G13.87. SCUBA fluxes are shown as squares: fluxes at 450 and 850μm are integrated over the map, whereas the 1350 and 2000μm fluxes are single pixel measurements and effectively lower limits. Other datapoints are near-IR (+) (Chini et al. 1987), IRAS 12-100μm (triangles); and 1300μm ($\times$) (Chini et al. 1986a,b).

the SCUBA fluxes were integrated is comparable to the IRAS beam at longer wavelengths. The 1350 and 2000μm points were single beam measurements and are effectively lower limits. Uncertainties on the radial profiles are from the noise on the map only and do not take into account strong asymmetries (such as multiple cores) in the SCUBA maps, or variation in the beam shape between the Uranus observations used to convolve the models and the actual beam shape for the source observations.

The model parameters are given in Table 4. The central radiation field is black body with temperature 42,000 K, equivalent to an 06 star (the exact temperature of the star has little effect on the SED, which is all reprocessed flux). We assume MRN grains throughout. The shell inner radius is set by its temperature, which we take as 300 K throughout (similar to Faison et al. (1998) and CWW90). The significance of this inner temperature and the effect of changing it is discussed further below. The temperatures at the outer edge are also given in Table 4, and at 10–20 K are typical of ambient molecular cloud material. For each source, the shell thickness (or outer radius) is chosen to fit the observed radial profile. The fits were carried out by eye from a limited range of models: current computing resources preclude running DUSTY for more than a few carefully chosen sets of input parameters. The SEDs for G13.87 and G43.89 were fitted by a combination of $\tau_{100\mu\mathrm{m}} = 0.1$ and 0.9 $r^{-3/2}$ SEDs contributing to the bolometric luminosity in proportion 1:1 (G43.89) and 2:3 (G13.87).

4.3. $r^{-3/2}$ models with cores

The peaked sources – G10.47, G12.21, and G31.41 – cannot be fitted simply by $r^{-3/2}$ distributions. At small radii, the observed emission falls off too steeply. Comparison with Uranus profiles suggests it is more consistent with a compact central source of dimensions much smaller than the beam. Also motivated by the knowledge that these sources have molecular hot cores, we consider the addition of a compact high column density core component to an $r^{-3/2}$ outer envelope similar to the $r^{-3/2}$ distributions used to fit the non-peaked sources.

These cores must be compact (much smaller than the beam) from the radial profiles, but as the cores are unresolved, the exact radial distribution is poorly constrained. From the relative fluxes in the peak/extended components of the images, the core

contributes less than $1/4$ as much submm flux as the total $r^{-3/2}$ contribution to the SED. This enables us to rule out cores with SEDs which peak shorter than 100μm, as these produce FIR fluxes in excess of the IRAS measurements when scaled to contribute enough flux in the submm. To produce a long-wavelength dominated SED from a compact core requires very high optical depths as the material must lie close to the heating source in order to emit enough flux; the more centrally condensed the distribution, the higher the optical depth.

If we identify the submm cores with hot molecular cores, then the molecular line observations provide some constraints on the parameters of the cores. From molecular line observations, column densities in hot cores exceed 10^{24}cm^{-2} and may reach 10^{25}cm^{-2} (Cesaroni et al. 1992, 1994a; Hatchell et al. 1998a); assuming a 100μm absorption coefficient $\kappa_{100\mu\mathrm{m}} = 2.9 \times 10^{-24}$cm^{-2}H atom^{-1} (Wolfire & Churchwell 1994) this corresponds to $\tau_{100\mu\mathrm{m}} \sim 3$–30. For our compact core component, as the radial distribution is poorly constrained from the profiles, we use a constant density model with $\tau_{100\mu\mathrm{m}} = 10$ and a core radius of $\sim 2''$, consistent with the measured molecular line column densities and source sizes (Cesaroni et al. 1992, 1994a; Hatchell et al. 1998a).

Fig. 6 shows the radial profile of this core (convolved with the beam) together with the observed profiles of G10.47 which is a peaked source. The core model fits the central peak well but falls away too fast; an additional extended component is needed. An obvious candidate is an $r^{-3/2}$ envelope like that used to fit the non-peaked sources. However, a spherically symmetric model with a single dense central core, modelled as a break in the radial density distribution, cannot reproduce the SEDs. With all the radiation from the star processed through the core, such a model produces a shortfall of flux at short wavelengths. In order to avoid this, we assume that the cores are not centrally positioned in the envelopes and are independently heated from the envelopes for the purposes of the modelling. The geometry we envisage places the core within a few arcseconds of the star which heats the envelope, at or near the inner edge of the envelope. The cores must be close to the envelope heating sources, and for the radial distribution modelling, we have assumed the centres are indistinguishable with our $9''/15''$ beam. This geometry leaves low optical depth paths from the envelope heating source which can account for the mid-IR fluxes.

Again, we are limited to combining spherical solutions for our models. By forming linear combinations of the SEDs, effectively we neglect the effect on the core SED of obscuration by envelope material along the line of sight. The amount of obscuration would depend on the exact (unknown) position of the core relative to the envelope heating star, and this would modify the exact shape of the core SED. However, our core SEDs are very approximate in shape anyway as we know very little about the size and density distribution of the cores. The important characteristics of the core SED - that it peaks longward of 100μm and contributes strongly at submm wavelengths - will not be altered even by obscuration by an envelope that is optically thick out to 100μm.

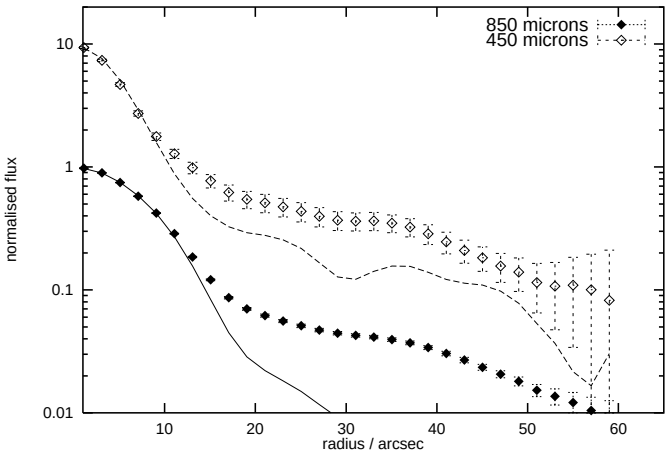

Fig. 6. Core model (without envelope) at 450μm (dashed line) and 850μm (solid line) compared with observed profiles (errorbars) for the peaked source G10.47.

Fig. 7 shows the SED and radial profile fits to the peaked sources G10.47, G12.21 and G31.41. In each case the fit is a combination of two $r^{-3/2}$ envelope components with optical depths of $\tau_{100\mu\mathrm{m}} = 0.3\mathrm{and}0.9$, plus a compact core with $\tau_{100\mu\mathrm{m}} = 10$ as described above. The composition of the fit is shown for G10.47. As for the non-peaked sources, the outer radii of the $r^{-3/2}$ distributions were chosen to match the radial profiles. Again, the model parameters are given in Table 4. For each source, the $\tau_{100\mu\mathrm{m}} = 0.3$ and 0.9 components were combined in ratio 2:3. The proportions of luminosity attributed to core and envelope, which are strongly constrained by the radial profiles, were (core:envelope) 1:3 (G10.47), 3:17 (G12.21) and 7:13 (G31.41). The mismatch between the model and observed radial profiles 30–$40''$ from the central peak in G10.47 can be explained by the additional dust cores (Fig. 1).

The opacities from the 2–4μm Brα, Brγ and Pfγ lines as measured for G5.89 (CWW90), which lie in the range 2.5–5.6, are consistent with those of the low optical depth $r^{-3/2}$ models with which we fitted the SEDs, which have 2–4μm opacities of 1.0–3.1 ($\tau_{100\mu\mathrm{m}} = 0.1$) and 2.9–9.4 ($\tau_{100\mu\mathrm{m}} = 0.3$).

4.4. Other models

The $r^{-3/2}$ and $r^{-3/2}$ plus core combinations that we have shown in Figs. 5 and 7 are chosen to produce a reasonable fit to the data with as few components as possible. The combinations are possibly not unique. Also the models have been chosen by eye by combining a limited number of models, and not by iterating through the parameter space to select models according to some best fit criterion. Therefore we hesitate to place too much weight on the exact values of parameters that we used, as there is a risk of overinterpretation. However, in our experience it is quite difficult to produce fits to both the SED and the radial distributions simultaneously, and while a few parameters are poorly constrained, certain areas of parameter space can be ruled out.

In Sect. 4.1 we noted that flat density distribution envelopes fail to fit the submm radial profiles. Fig. 8 shows that r^{-2} and

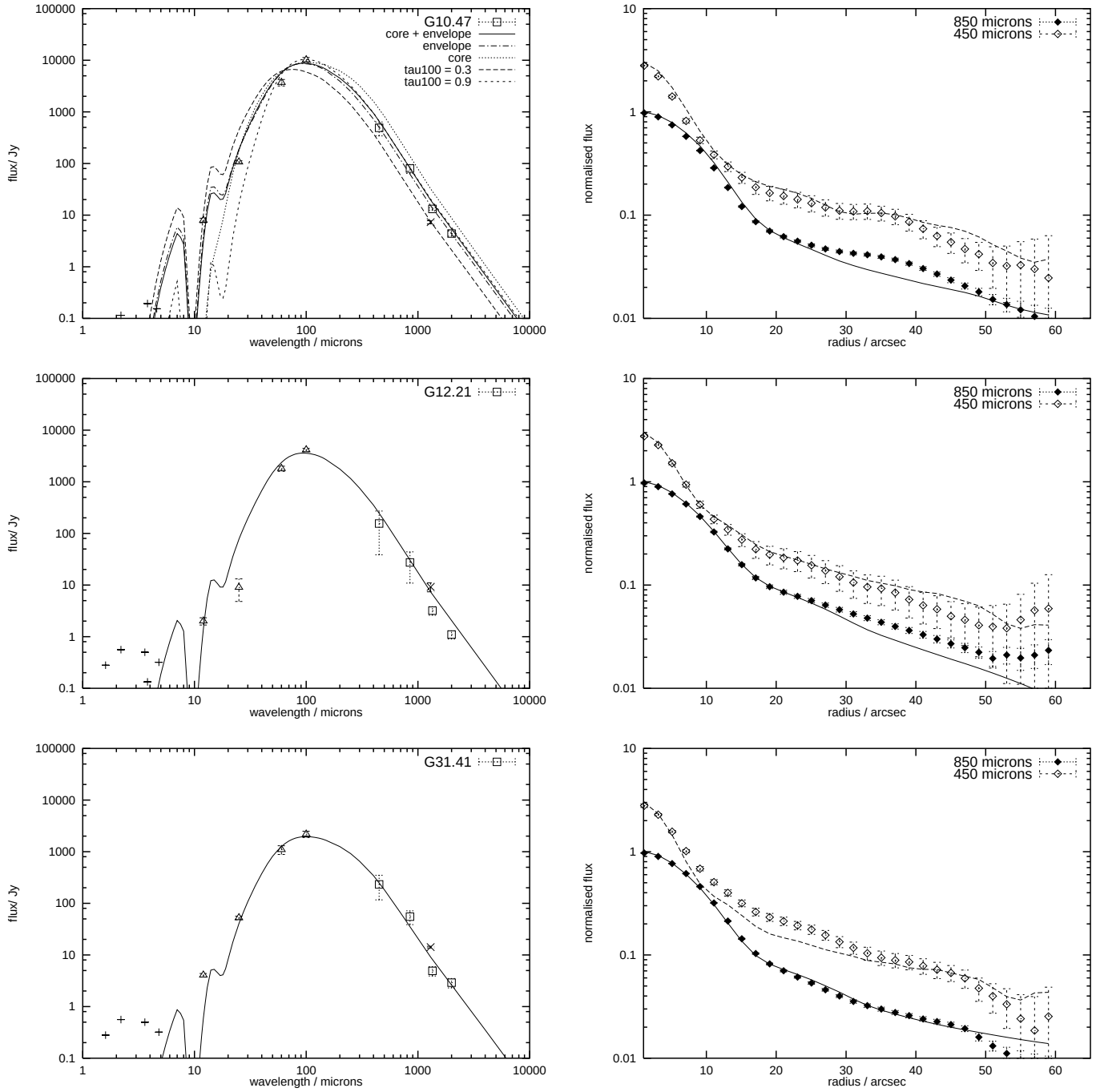

Fig. 7. SEDs and radial profiles for the peaked sources G10.47 (top), G12.21 (middle) and G31.41 (bottom), fitted by $r^{-3/2}$ envelopes plus compact cores. The SED for G10.47 shows the combination of $r^{-3/2}$ $\tau_{100\mu\mathrm{m}} = 0.3$ and $\tau_{100\mu\mathrm{m}} = 0.9$ models to form the envelope SED, plus a compact core, used to form the final SED. SCUBA fluxes are shown as squares: fluxes at 450 and 850μm are integrated over the map, whereas the 1350 and 2000μm fluxes are single pixel measurements and effectively lower limits. Other datapoints are near-IR ($+$) (Chini et al. 1987), IRAS 12-100μm (triangles); and 1300μm ($\times$) (Chini et al. 1986a,b).

r^{-1} density distributions have too steep and too shallow radial profiles, respectively, for the envelope.

For both envelope and core, we have taken the dust temperature at the inner radius of the shell to be 300 K. The exact temperature is not well constrained but we can rule out inner temperatures consistent with dust sublimation temperatures of $\gtrsim 1000\ K$, or too much short wavelength emission is produced. Similarly low temperatures were required by CWW90 and Faison et al. (1998) for their constant density fits to the SED, and the problem is worse for more centrally condensed $r^{-3/2}$ density distributions. Fig. 9 shows SEDs for a $r^{-3/2}$ envelope with an inner temperature of 1000 K and two optical depths, and data

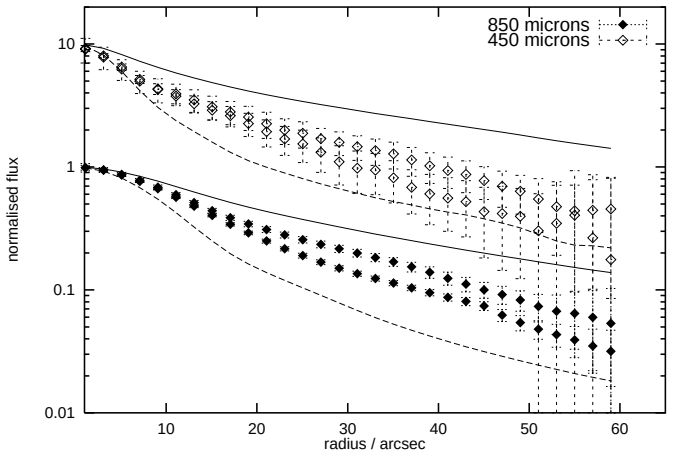

Fig. 8. r^{-1} (solid) and r^{-2} (dashed) density models compared with 450 and 850μm radial profiles of the two non-peaked sources G13.87 and G43.89.

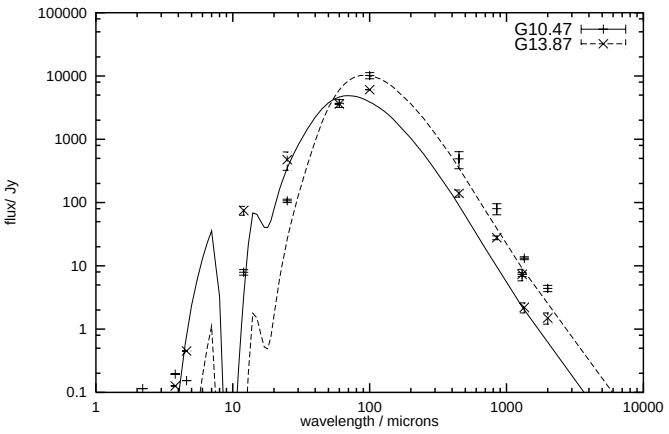

Fig. 9. SED of $r^{-3/2}$ model with 1000 K inner temperature for $\tau_{100\mu\mathrm{m}} = 1.0$ (solid) and 3.0 (dashed) compared with observed fluxes for G10.47 and G13.87 (errorbars).

from G13.87 and G10.47. 1–20μm data for these sources would provide better constraints, but even for the lower optical depth model the silicate feature is much stronger than other similar sources (Faison et al. 1998), and the 2-4μm optical depths of 10–40 are much larger than the 2–6 observed in G5.89 (CWW90).

5. Discussion

The main results of the modelling are that a $r^{-3/2}$ density distribution, plus in some cases a compact, high column density core, fits both SEDs and radial brightness distributions; and that the peaked sources which required compact cores in the modelling are also those identified as molecular line rich in our hot core survey (Hatchell et al. 1998a), as noted in Sect. 3. In this section we discuss the constraints which the models place on the source properties, compare the dust models with the molecular line data, and discuss the effect of grain opacity.

5.1. Source properties

We showed in Sect. 4 that the envelope density distribution is well constrained by the data: a $r^{-3/2}$ distribution fits the radial intensity profiles of the non-peaked sources better than constant, r^{-1} or r^{-2} density distributions, and that the same $r^{-3/2}$ envelope can be combined with a compact, optically thick core to produce the profiles for the peaked sources.

It is unclear what is setting the inner radius of the dust shells. Our models also require a low dust temperature of ~ 300 K on the inner boundary, in agreement with the previous spherical dust models, in order to limit the short wavelength emission (CWW90; Faison et al. 1998). A boundary set by dust sublimation, expected at > 1000 K, appears to be ruled out by such low temperatures. Presumably the inner radius is set by either radiation pressure or stellar/disk winds.

The luminosity of the driving source(s) is constrained by the total flux emitted across all wavelengths. This can be estimated from the data by interpolation between the observed fluxes and integrating. Alternatively, the total flux can be taken from the combination of models used to fit the SED. For the sources observed here, Churchwell et al. (1990b) gave luminosities based on those produced by WC89 using the first method, corrected for revised distances. These flux estimates did not take into account the flux emitted outside the IRAS bands, which WC89 suggest may be as much as 50%. With the inclusion of the submm data, and using the models to fit the SED, we have revised luminosity estimates for G10.47, G12.21 and G43.89, which are listed in Table 5 along with the corresponding spectral type assuming a single driving source (although we cannot distinguish single sources from clusters).

Table 5. Revised luminosities and corresponding spectral types (from Panagia 1973).

Source	$\log_{10}(L/L_\odot)$	Spectral type
G10.47	5.60	05.5
G12.21	5.95	05
G13.87	5.23	06.5
G31.41	5.23	06.5
G43.89	4.60	09.5

As noted in Sect. 4.2, few of the core properties are well constrained. The cores must have size much less than the beamsize and a high optical depth. The radial distribution of the compact cores are poorly constrained; higher resolution observations would be of use here. Interferometric continuum observations of G10.47 and G31.41 suggest that these cores have diameters of $1.3''$ and $0.98''$ respectively (Cesaroni et al. 1994b; Olmi et al. 1996a), which is slightly smaller than our model cores. The relative contribution to the submm flux, which is constrained by the radial profile, determines the relative luminosity of core and envelope once SED models for each are chosen. In fact the cores may be flattened, or even disks.

Limits on core luminosities in the non-peaked sources G13.87 and G43.89 are 1–2% of the total; with any more flux in a core component the radial profile fails to fit the observations.

Our modelling assumes that the cores are heated independently from the UCHII regions, by internal sources, but external heating is also a possibility. Whether the UCHII driving sources can also provide enough flux to the cores can be settled by geometric arguments, if the relative positions of the star (in the UCHIIregion) and the cores are known. The cores provide $1/6$–$1/4$ of the total flux; if they and the extended envelopes are heated by the same star then the cores must fill $1/6$–$1/4$ of the solid angle surrounding the star. For a $4''$ diameter core, the core has to be within $2''$ of the star in order to capture sufficient flux. Higher angular resolution observations are required to determine the relative positions of UCHII driving source and dust core. Of the sources studied here, interferometric observations show that the G10.47 molecular core may satisfy this criterion, with the ammonia core surrounding the UCHII region at a distance of $\lesssim 1''$ (assuming the line joining star and core lies within $60\,\mathrm{deg}$ of the plane of the sky), but in G31.41 the molecular core is $4''$ from the UCHII regions and must be separately powered (Cesaroni et al. 1998). Another argument against externally heated cores is that it is difficult to produce large amounts of hot gas (Kaufman et al. 1998). This does not conflict with the submm continuum observations, as enhanced emission at 450/850μm can be explained by dust at only a few tens of kelvin. But the detection of high column densities of highly excited molecular species such as methyl cyanide and ammonia (eg. Hatchell et al. 1998a; Cesaroni et al. 1992; Olmi et al. 1993) suggest that there are large amounts of hotter dust in the cores, which is naturally produced if the heating is internal rather than external. Such high-luminosity internally-heated cores without detectable UCHII regions are presumably massive protostars.

5.2. Comparison with molecular line data

The sources which required the addition of compact cores in order to model the radial density distributions were G10.47, G12.21 and G31.41, whereas G13.87 and G43.89 did not. In our molecular line survey towards UCHII regions (Hatchell et al. 1998a) we also differentiated between these groups of sources on the basis of their molecular line emission. G10.47, G12.21 and G31.41 were line-rich hot core sources, showing high abundances of grain ice evaporated species and their daughter products. The molecular lines showed evidence for a hot, dense core surrounded by a cooler envelope. Neither G13.87 nor G43.89 had a rich molecular line spectrum, and Hatchell et al. (1998a) concluded that neither contained a hot molecular core. The SCUBA results confirm the need for compact cores in G10.47, G12.21 and G31.41, but not G13.87 or G43.89. We identify the compact cores in the SCUBA dust continuum images with the hot molecular cores identified from their molecular line emission.

SCUBA is therefore an excellent instrument for identifying hot core sources, because the high sensitivity array results in high dynamic range images after short integrations (here just over a minute per source), and only basic removal of bad pixels is required to produce a radial distribution plot from which the sources with hot cores can be identified by their steep profiles.

Column densities and masses calculated from the models are given in Table 4. For both core and envelope these are consistent with molecular line data. The $r^{-3/2}$ model masses of a few times $10^4 M_\odot$ correspond to a few times 10^2–$10^3 M_\odot$ in a single 15–$20''$ beam, consistent with measurements of 10^2– a few times$10^3 M_\odot$ from $C^{17}O/C^{18}O$ and $C^{34}S$ measurements (Hatchell et al. 1998a; Cesaroni et al. 1991). Column densities of 7×10^{23} cm^{-2} agree well with what is measured in CO.

Another difference between sources with and without cores is apparent when considering just the envelopes. The $r^{-3/2}$ envelopes of the sources with cores have higher column densities and higher masses than the coreless sources. There may be a mass cutoff of $\sim 2 \times 10^4 M_\odot$ below which cores do not form.

Temperatures within the envelopes fall off rapidly. Only the inner 1–$2''$ of the envelopes remains at temperatures above 100 K, in the radiative transfer models; at a radius of $5''$ the temperature has dropped to below 50 K. The temperatures at the outer edges of the envelopes are 10–20 K, typical of quiescent dense cloud material (envelope outer radii are 70–$160''$ – see Table 4).

Core masses from the dust model, of a few times $10^3 M_\odot$, are larger than virial mass estimates of a few hundred to $1000 M_\odot$ from warm, dense gas tracers CH_3CN, CH_3OH and NH_3 (Hatchell et al. 1998a; Cesaroni et al. 1992), and from NH_3 interferometry in G10.47 and G31.41 (Cesaroni et al. 1994a), by a factor of a few. 3mm interferometry estimates for the cores are $2000 M_\odot$ for G10.47 (Olmi et al. 1996a) and $\sim 1000 M_\odot$ for G31.41 (Cesaroni et al. 1994b). Again the column densities of $\sim 10^{25}$ cm^{-2} compare well with estimates from molecular lines. As mentioned above, the core model is only approximate as the parameters are not well constrained by the observations. Smaller cores could reduce the mass without reducing the column density, but also shift the spectrum to shorter wavelengths. It may be possible to reconcile this with the SED: the core emission is reduced at shorter wavelengths by the envelope optical depth (see Sect. 4.3), and a grain model with relatively high submm opacity could be used. A reduction in optical depth, or a simple increase in grain opacity (corresponding to icy or bare coagulates: see discussion of grain properties below) would reduce both mass and column density. Alternatively, the larger model masses may be explained if the cool, ~ 50 K, outer parts of the cores are poorly traced by the high excitation molecular lines of CH_3OH and CH_3CN, or if the assumption of virial equilibrium is invalid.

The molecular line emission itself will contribute to the broad band submm flux. Although some molecular line survey data exists for the sources considered in this paper, the frequency coverage is such a small fraction of the total SCUBA bands that a source-by-source calculation of the line contribution is not possible. Sutton et al. (1984) estimate that as much as 45-60% of the 215–247 GHz flux in Orion, when measured with an $36''$ beam, is due to line emission. The line contribution from the outer envelope will be small because the molecular lines are

few and weak (Thompson et al. 1999) but the chemically active hot cores have rich molecular spectra and line emission will contribute significantly to the fluxes at the peaks. A comparison of the single-beam fluxes and map fluxes (Table 3) shows that 30–50% of the submm flux integrated over the map can be attributed to the cores. A possible 60% enhancement in flux as measured with a large beam could therefore explain the appearance of peaked sources in the submm as wholly due to molecular line emission. In practice, the large column densities of molecular gas required to produce these line fluxes are likely to coexist with an equivalent quantity of dust: processes that destroy or remove the dust would also destroy or remove the molecules, and many of the molecular species observed rely on icy grain mantles for their production, indicating the presence of dust. Nevertheless, the core emission which we have modelled as due to dust alone may in fact be due to a combination of dust and molecular line emission.

5.3. Grain properties

The model SEDs depend on the dust opacities assumed, which are poorly known at long wavelength. The spectral index β for the opacity above 100μm ($\kappa_\lambda \propto \lambda^{-\beta}$) is expected to lie in the range 1–2. Theory suggests $\beta = 2$ for crystalline materials (Draine & Lee 1984; Ossenkopf et al. 1992) and $\beta = 1$ for amorphous carbon (Hanner 1988; Jäger et al. 1998). As well as the spectral index, the actual value of the opacity at 100μm varies depending on the type of grain, including whether or not it has an ice mantle. The models here follow CWW90 in calculating the opacity assuming Mie scattering from the Draine & Lee (1984) optical properties for a mixture of graphite and silicon, giving $\kappa_{100\mu\mathrm{m}} = 6.4 \times 10^{-25}$ cm^2(H atom)$^{-1}$ for ice-free grains with $\beta = 2$.

Coagulated grains with or without ice increase $\kappa_{100\mu\mathrm{m}}$ (Ossenkopf & Henning 1994). Hence, masses and column densities could be reduced by a factor of a few for the same optical depths. Using a coagulated grain model would also affect the shape of the spectrum, producing more submm emission for the same infrared flux. This might enable the SEDs to be fitted with lower near- and mid-IR optical depths. Because the 1350/2000μm points are single-beam and therefore effectively lower limits, the mm/submm data is not sufficent to differentiate between $\beta = 1$ and $\beta = 2$ opacity models.

6. Conclusions

We have imaged the submm emission towards five high mass star formation regions using SCUBA on the JCMT, and modelled the resulting spectral energy distributions and radial profiles as emission from spherically symmetric dust shells.

- The images show strong emission peaks towards known UCHII positions in all cases. In G10.47 and possibly G12.21 there are further dust emission peaks without known UCHII.
- Some sources show more strongly centrally peaked emission than others. The peaked sources are those previously identified from spectral line observations as having hot molecular cores. Sources with hot cores can be identified much faster using SCUBA submm images than from spectral line observations.
- The spectral energy distributions and radial brightness profiles can be modelled by dust distributions with a $r^{-3/2}$ density profile, plus the addition of a compact, high column density core in three out of five sources (G10.47, G12.21 and G31.41). The sources which required compact cores to fit the dust emission are the peaked, hot molecular core sources.
- The inner boundary of the dust shells appears to be set by something other than dust sublimation, as low temperatures of only a few hundred kelvin at the inner boundary are required to fit the SEDs. The physical mechanism which sets the inner boundary is unclear.

Acknowledgements. We are indebted to Željko Ivezić, Maia Nenkova and Moshe Elitzur for making the DUSTY radiative transfer code freely available. We would like to thank the JCMT staff, particularly Iain Coulson who carried out the observations and preliminary data reduction for us, and an anonymous referee for their thoughtful criticism. Research at UMIST is supported by the UK Particle Physics and Astronomy Research Council (PPARC). The JCMT is operated by the Joint Astronomy Centre on behalf of the PPARC, the Netherlands Organisation for Scientific Research, and the National Research Council of Canada.

References

Aliakberov K.D., Berlin A.B., Gol'nev V.Y., et al., 1985, AZh 62, 482
Anglada G., Estalella R., Pastor J., Rodriguez L.F., Haschick A.D., 1996, ApJ 463, 205
Bachiller R., Menten K.M., Gonzalez J., Barcia A., 1990, A&A 240, 116
Baudry A., Desmurs J.F., Wilson T.L., Cohen R.J., 1997, A&A 325, 255
Becker R.H., White R.L., Helfand D.J., Zoonematkermani S., 1994, ApJS 91, 347
Brand J., Cesaroni R., Caselli P., et al., 1994, A&AS 103, 541
Braz M.A., Epchtein N., 1983, A&AS 54, 167
Bronfman L., Nyman L.-A., May J., 1996, A&AS 115, 81
Caswell J.L., 1998, MNRAS 297, 215
Caswell J.L., Gardner F.F., Norris R.P., et al., 1993, MNRAS 260, 425
Caswell J.L., Vaile R.A., Ellingsen S.P., 1995a, PASA 12, 37
Caswell J.L., Vaile R.A., Ellingsen S.P., Norris R.P., 1995b, MNRAS 274, 1126
Caswell J.L., Vaile R.A., Ellingsen S.P., Whiteoak J.B., Norris R.P., 1995c, MNRAS 272, 96
Caswell J.L., Vaile R.A., Forster J.R., 1995d, MNRAS 277, 210
Cesaroni R., Walmsley C.M., Kömpe C., Churchwell E., 1991, A&A 252, 278
Cesaroni R., Walmsley C.M., Churchwell E., 1992, A&A 256, 618
Cesaroni R., Churchwell E., Hofner P., Walmsley C.M., Kurtz S., 1994a, A&A 288, 903
Cesaroni R., Olmi L., Walmsley C.M., Churchwell E., Hofner P., 1994b, ApJ 435, 137
Cesaroni R., Hofner P., Walmsley C.M., Churchwell E., 1998, A&A 331, 709
Chini R., Kreysa E., Mezger P. G., Gemünd H.-P., 1986a, A&A 154, L8

Chini R., Kreysa E., Mezger P. G., Gemünd H.-P., 1986b, A&A 157, L1
Chini R., Krügel E., Wargau W., 1987, A&A 181, 378
Churchwell E., Walmsley C.M., Cesaroni R., 1990b, A&AS 83, 119
Churchwell E., Wolfire M.G., Wood D.O.S., 1990a, ApJ 354, 247 (CWW90)
Churchwell E., Walmsley C.M., Wood D.O.S., 1992, A&A 253, 541
Codella C., Palumbo G.G.C., Pareschi G., et al., 1995, MNRAS 276, 57
Cohen R.J., Masheder M.R.W., Walker R.N.F., 1991, MNRAS 250, 611
Cox P., 1990, A&A 236, 29
Doherty R.M., Puxley P., Doyon R., Brand P.W.J.L., 1994, MNRAS 266, 497
Draine B.T., Lee H.M., 1984, ApJ 285, 89
Dyson J.E., Williams R.J.R., Redman M.P., 1995, MNRAS 277, 700
Faison M., Churchwell E., Hofner P., et al., 1998, ApJ 500, 280
Feldt M., Stecklum B., Henning Th., Launhardt R., Hayward T.L., 1999, A&A 346, 243
Feldt M., Stecklum B., Henning Th., et al., 1998, A&A 339, 759
Forster J.R., Caswell J.L., 1989, A&A 213, 339
Forster J.R., Goss W.M., Gardner F.F., Stewart R.T., 1985, MNRAS 216p, 35
Furst E., Reich W., Reich P., Reif K., 1990, A&AS 85, 805
Garay G., Moran J.M., Rodriguez L.F., 1993a, ApJ 413, 582
Garay G., Rodriguez L.F., Moran J.M., 1993b, Rev. Mex. Astron. Astrofis. 26, 95
Garay G., Rodriguez L.F., Moran J.M., Churchwell E., 1993c, ApJ 418, 368
Garay G., Lizano S., Gomez Y., 1994, ApJ 429, 268
Gaume R.A., Mutel R.L., 1987, ApJS 65, 193
Gaylard M.J., Macleod G.C., Van der Walt D.J., 1994, MNRAS 269, 257
Gensheimer P.D., Mauersberger R., Wilson T.L., 1996, A&A 314, 281
Griffith M.R., Wright A.E., Burke B.F., Ekers R.D., 1994, ApJS 90, 179
Handa T., Sofue Y., Nakai N., Hirabayashi H., Inoue M., 1987, PASJ 39, 709
Hanner M.S., 1988, NASA Conf. Pub. 3004, 22
Hatchell J., Thompson M.A., Millar T.J., Macdonald G.H., 1998a, A&AS 133, 29
Hatchell J., Thompson M.A., Millar T.J., Macdonald G.H., 1998b, A&A 338, 713
Hatchell J., Millar T.J., Rodgers S.D., 1998c, A&A 332, 695
Hatchell J., Roberts H., Millar T.J., 1999, A&A 346, 227
Hoare M.G., Roche P.F., Glencross W.M., 1991, MNRAS 251, 584
Holland W.S., Robson E.I., Gear W.K., et al., 1999, MNRAS 303, 659
Hofner P., Churchwell E., 1996, A&AS 120, 283
Ivezić Ž., Elitzur M., 1997, MNRAS 287, 799
Ivezić Ž., Nenkova M., Elitzur M., 1997, User Manual for DUSTY. Internal Report, University of Kentucky (accessible at http://www.pa.uky.edu/∼moshe/dusty)
Jaffe D.T., Güsten R., Downes D., 1981, ApJ 250, 621
Jaffe D.T., Stier M.T., Fazio G.G., 1982, ApJ 252, 601
Jäger C., Mutschke H., Henning Th., 1998, A&A 332, 291
Jenness T., Lightfoot J.F., 1998, In: Albrecht R., Hook R.N., Bushouse H.A. (eds.) Astronomical Data Analysis Software and Systems VII, ASP Conf. Ser. 145, p. 216
Jourdain de Muizon M., Cox P., Lequeux J., 1990, A&AS 83, 337
Kalenskij S.V., Bachiller R., Berulis I.I., et al., 1992, AZh 69, 1002
Kaufman M. J., Hollenbach D.J., Tielens A.G.G.M., 1998, ApJ 497, 276
Kemball A.J., Diamond P.J., Mantovani F., 1988, MNRAS 234, 713
Koo B.-C., Williams D.R.W., Heiles C., Backer D.C., 1988, ApJ 326, 931
Kwok S., Volk K., Bidelman W.P., 1997, ApJS 112, 557
Lizano S., Canto J., Garay G., Hollenbach D., 1996, ApJ 468, 739
Lockman F.J., 1989, ApJS 71, 469
Mathis J.S., Rumpl W., Nordsieck K.H., 1977, ApJ 217, 425 (MRN)
Mehringer D.M., Goss W.M., Palmer P., 1995, ApJ 452, 304
Menten K.M., 1991, ApJ 380, 75
Moorwood A.F.M., Salinari P., 1981, A&A 94, 299
Nummelin A., Dickens J.E., Bergman P., et al., 1998, A&A 337, 275
Olmi L., Cesaroni R., Neri R., Walmsley C.M., 1996a, A&A 315, 565
Olmi L., Cesaroni R., Walmsley C.M., 1996b, A&A 307, 5990
Olmi L., Cesaroni R., Walmsley C.M., 1993, A&A 276, 489
Olnon F.M., Raimond E., IRAS science team, 1986, A&AS 65, 607
Ossenkopf V., Henning Th., 1994, A&A 291, 943
Ossenkopf V., Henning Th., Mathis J.S., 1992, A&A 261, 567
Palagi F., Cesaroni R., Comoretto G., Felli M., Natale V., 1993, A&AS 101, 153
Panagia N., 1973, AJ 78, 929
Plume R., Jaffe D.T., Evans N.J. II, 1992, ApJS 78, 505
Redman M.P., Williams R.J.R., Dyson J.E., 1998, MNRAS 298, 33
Redman M.P., Williams R.J.R., Dyson J.E., 1996, MNRAS 280, 661
Reich W., Reich P., Furst E., 1990, A&AS 83, 539
Roellig M., Kegel W.H., Mauersberger R., Doerr C., 1999, A&A 343, 939
Sandell G., 1997, The SCUBA mapping cookbook. CCLRC / Rutherford Appleton Laboratory/Particle Physics & Astronomy Research Council
Schutte A.J., van der Walt D. J., Gaylard M.J., Macleod G.C., 1993, MNRAS 261, 783
Scoville N.Z., Yun M.S., Clemens D.P., Sanders D.B., Waller W.H., 1987, ApJS 63, 821
Shepherd D.S., Churchwell E., 1996, ApJ 457, 267; 1984, ApJ 283, 41
Simpson J.P., Rubin R.H., 1990, ApJ 354, 165
Sutton E.C., Blake G.A., Masson C.R., Phillips T.G., 1984, ApJ 283, L41
Tang G.-S., Sun J., Lu J., 1996, Acta Astron. Sin. 37, 404
Tenorio-Tagle G., 1977, A&A 54, 517
Testi L., Felli M., Persi P., Roth M., 1998, A&AS 129, 495
Thompson M.A., Macdonald G.H., Millar T.J., 1999, A&A 342, 809
van der Walt D.J., Gaylard M.J., Macleod G.C., 1995, A&AS 110, 81
Volk K., Cohen M., 1989, AJ 98, 931
Walsh A.J., Hyland A.R., Robinson G., Burton M.G., 1997, MNRAS 291, 261
Williams R.J.R., Dyson J.E., Redman M.P., 1996, MNRAS 280, 667
Wink J.E., Wilson T.L., Bieging J.H., 1983, A&A 127, 211
Wood D.O.S., Churchwell E., 1989, ApJS 69, 831 (WC89)
Wood D.O.S., Handa T., Fukui Y., et al., 1988, ApJ 326, 884
Wolfire M.G., Churchwell E., 1994, ApJ 427 889
Wouterloot J.G.A., Brand J., Fiegle K., 1993, A&AS 98, 589
Wyrowski F., Walmsley C.M., 1996, A&A 314, 265
Wyrowski F., Schilke P., Walmsley C.M., 1999, A&A 341, 882
Zavagno A., Cox P., Baluteau J.P., 1992, A&A 259, 241
Zheng X.-W., Ling Z.-F., 1997, Acta Astron. Sin. 38, 135
Zoonematkermani S., Helfand D.J., Becker R.H., White R.L., Perley R.A., 1990, ApJS 74, 181